THE JOURNAL OF PHYSICAL CHEMISTRY C

pubs.acs.org/JPCC Article

Charging Amorphous Solid Water Films by Ne^+ Ions Characterized by Contact Potential Difference Measurements

Michelle Akerman, Roey Sagi, and Micha Asscher*

Cite This: J. Phys. Chem. C 2020, 124, 23270–23279 Read Online

ACCESS | Metrics & More | Article Recommendations

ABSTRACT: The study of amorphous solid water (ASW) films on solid substrates has been instrumental in understanding the structure and morphology of water ices. In addition, they have the potential to help researchers understand how complex molecules are formed in regions of the interstellar medium (ISM) where many surfaces are coated with ASW. We have studied ASW films charged by low-energy Ne^+ ions under ultrahigh vacuum conditions by measuring the contact potential difference of the charged films with a Kelvin probe. The film becomes positively charged when impinging Ne^+ ions oxidize the surface water molecules and subsequently scatter back to the vacuum as neutral Ne atoms. The charged ASW film follows plate capacitor physics, displaying a linear dependence of voltage on ASW layer thickness. Electrical fields of 2 $(\pm 1) \times 10^8$ V/m are generated within the films. The level of charging, charge stability, and thermal binding energy of the charges to the ASW film are all very sensitively dependent on the film growth temperature and the temperature of the film during Ne^+ ion impingement. We propose that these properties are affected by the film's porosity and the nature of the proton binding sites, which are dictated by the film growth temperature. The protons are trapped in undercoordinated water molecule defect sites and L-defect sites, with thermal binding energies ranging from 3.4 to 9.4 kcal/mol, as determined by differential contact potential difference $(d(\Delta CPD)/dT)$ measurements, obtained during sample annealing.

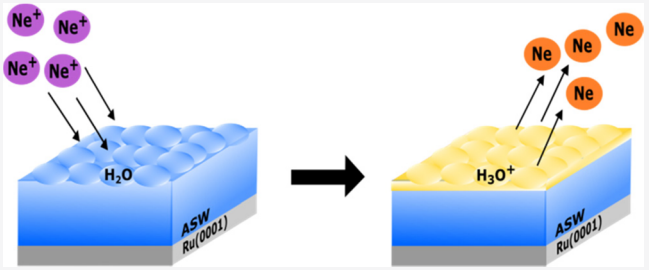

1. INTRODUCTION

Amorphous solid water (ASW) is thought to be the most abundant form of water in the universe. In the solar system, layers of ASW coat surfaces of satellites, rings, and dust particles that are colder than 140 K. While ice is mostly comprised of water, it also contains other simple molecules, such as CH_3OH, NH_3, CO, CO_2, and CH_4[1,2] at densities equal to or smaller than 10% of the density of water. The icy layers are subject to bombardment by electrons, cosmic rays (positive charges), and UV photons. UV irradiation of the icy mantles leads to the formation of an abundance of free radicals[3] that can combine to form large organic molecules, including amino acids.[4] If the icy objects are cold enough, bombardment by positively or negatively charged particles could lead to stable electrostatic charging, generating strong electric fields inside the ice layers.

Electric fields can affect the reactivity and selectivity of chemical reactions.[5−7] External electric fields were theoretically predicted to stabilize transition states and induce dipole alignment, enabling reactions that would otherwise not be possible due to energetic or geometrical constraints. Shin et.al have demonstrated how an ice nanocapacitor generates strong electric fields in condensed films.[8] This method has shown that water molecules can undergo a dipolar reorientation as seen by changes in their stretching and bending vibrational spectra[9,10] at temperatures as low as 10 K. Additionally, Coote and coworkers have demonstrated that radical stability and reactivity can be affected by an electric field.[11−13] These works suggest that the rich chemistry occurring on ASW-coated dust grains in the interstellar medium (ISM) may be significantly influenced by strong electric fields.

Positive and negative charging of both crystalline and amorphous water ice films has been extensively studied in recent years. When a water ice film is charged following collisions by positive ions[8,14−19] or electrons,[18,20−23] a strong electric field is generated within the film. Positive charging is obtained either via soft-landing of positively charged ions onto the water ice surface,[8,14] exposure to a low-energy ion beam (LEIB),[18] or bombardment with high-energy ions.[16,17,19] The positive charges have been used to study the dielectric properties of ASW,[14] proton transport in ASW,[19] and charging stability properties[16,17] and to utilize the electric fields for

Received: September 1, 2020
Revised: September 24, 2020
Published: October 13, 2020

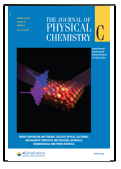

studying their effects on molecular systems.[8] Here, we use low-energy Ne^+ ions to charge ASW films in the temperature range of 35−120 K. The charged ASW film was characterized by employing a Kelvin probe to track the changes in the contact potential difference of the ASW films. We have studied the effects of ASW layer thickness, Ne^+ ion beam energy, and irradiation time on the charging level and stability. The nature of the charge binding sites was investigated by studying the effects of morphology (which is correlated to the ASW growth temperature) and irradiation temperature on their thermodynamics. These observations are discussed with their potential impact on processes occurring in the ISM.

2. EXPERIMENTAL METHODS

The experiments performed in this study were conducted in a previously described ultrahigh vacuum system[23,24] with a base pressure of 2×10^{-10} Torr. A Ru(0001) single-crystal substrate was attached to two Ta legs, 3 mm in diameter, via 0.4 mm Ta wires spot-welded to the top and bottom edges of the Ruthenium sample. The Ta legs were connected to a manipulator on a rotatable stage (McAllister) and a closed-cycle He cryostat (Janis) that cools the sample down to 30 K. The temperature was measured using a K-type thermocouple (chromel−alumel) spot-welded to one side of the sample, providing an accuracy of ± 1 K. The Ru(0001) substrate was cleaned daily by a 15 min sputter with 1000 eV Ne^+ ions followed by annealing at 1450 K for 180 s. ASW films were deposited on the Ru(0001) surface by backfilling the chamber with gaseous water until the desired film thickness was achieved. This ensured homogeneous water coverage of all cold surfaces around the sample, avoiding stray current measurements via uncovered conducting elements near the sample. The sample temperature was stabilized using a LakeShore 335 at temperatures in the range of 35−120 K. The ASW films were subsequently charged by bombardment with low-energy Ne^+ ions (1.28×10^{11} collisions/s) using an ion sputter gun (Varian) at low energies (typically 85 eV). The charging level and stability were evaluated by measuring the change in contact potential difference (ΔCPD) with a Kelvin Probe (KP S, Besocke Delta-PHI) upon completion of the charging process. Temperature-programmed ΔCPD (TP-ΔCPD) experiments and its derivative ($d(\Delta CPD)/dT$) were performed using a computer-controlled heating algorithm (LabView) that allows for gradual heating (or cooling) of the sample. The system is equipped with a quadrupole mass spectrometer (QMS, RGA 300, SRS) for performing temperature-programmed desorption (ΔP-TPD) measurements.

3. RESULTS AND DISCUSSION

3.1. Charging Mechanism. The collision of low-energy Ne^+ ions with ASW films leads to positive charging, creating a potential difference across the film that can be measured with a Kelvin probe. The Kelvin probe measures the contact potential difference (CPD) between the sample and an inert counter electrode, which is defined as the difference between the work function of the counter electrode and that of the sample. Typically, the sample is composed of a conducting substrate with a molecular adsorbate on its top. Positive charging is detected as a negative change in the CPD. During the charging process, a positive transmission current is detected on the Ruthenium sample, indicating that not all of the positive charges become trapped in the ASW film. Further discussion of this current and its meaning is beyond the scope of this article.

We propose that the film is positively charged through a charge-transfer mechanism in which the impinging Ne^+ ion ionizes a neutral water molecule near the surface of the ASW film. The first ionization energy for a neon atom is 21.6 eV[25] (we may assume here that the electron affinity of a positive ion, for example, Ne^+, to form a neutral atom is equivalent to the ionization potential of the neutral atom), significantly higher than the 11.0 eV ionization threshold for water ice.[26] Therefore, it is likely that when the impinging Ne^+ ion strikes the ASW film, it oxidizes a water molecule and becomes neutral. The excess energy is released (mostly) as heat within the ASW matrix. The following mechanism $Ne^+ + (H_2O)_n \rightarrow Ne + (H_2O)_n^+$ most likely describes the charge-transfer process. Another possible mechanism based on a previous study of low-energy (1−10 eV) proton−water ice collisions[27] is as follows

$$Ne^+ + 2H_2O_{(ad)} \rightarrow H_3O^+ + NeOH$$
$$\rightarrow Ne + OH + H_3O^+_{(ad)}$$

Upon the completion of the charging process, temperature-programmed desorption (TPD) measurements tracking mass 20 (Ne) show that a very small amount of neutral neon becomes trapped in the ASW surface sites and desorbs at ∼50 K (Figure 1). This peak was also observed for films exposed to

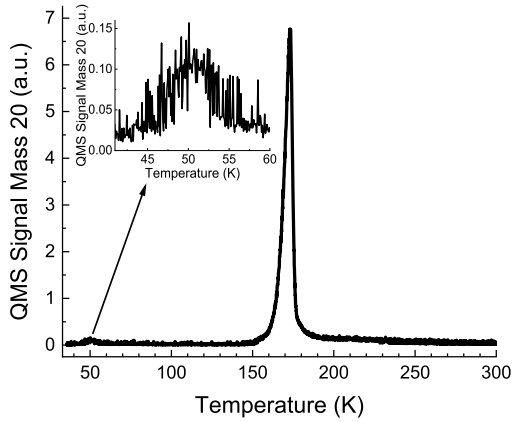

Figure 1. TPD measurement at m/z = 20 tracking neon atoms trapped in water films of 100 ML thickness following exposure to neon ions (85 eV, 8 nA) for 300 s.

neutral neon (at the same base pressure of 6×10^{-7} Torr), suggesting that the trapped neon is not a charge carrier. A second peak for mass 20 is observed at 160 K, where multilayer desorption of water occurs. The same peak (in temperature and intensity) is observed for an uncharged ASW film. Since D_2O also has a mass of 20, it is likely that the peak observed at 160 K corresponds to trace amounts of D_2O present in the ASW film (the intensity for mass 18 is orders of magnitude higher under the same conditions). This suggests that the neutral neon does not become trapped deep inside the ASW film. These TPD measurements confirm that most of the neon atoms desorb from the water film immediately following the ionization of surface water molecules. The mechanisms shown above suggest that the positive charge on the film is a proton (or H_3O^+). The protons are stabilized in traps in the ASW film.

https://dx.doi.org/10.1021/acs.jpcc.0c07969
J. Phys. Chem. C 2020, 124, 23270−23279

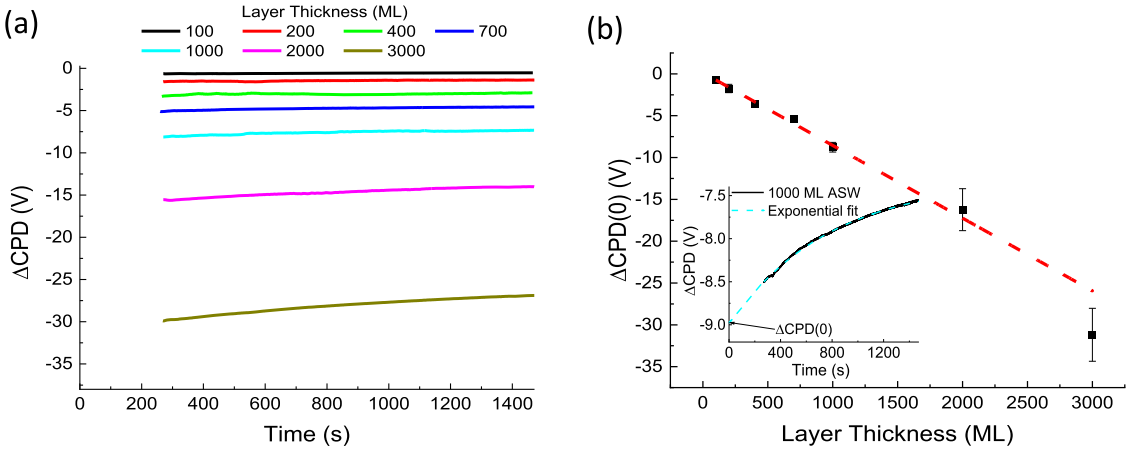

Figure 2. Effect of layer thickness on charging level and stability. (a) ΔCPD measured over a 20 min period. The first 4.5 min cannot be recorded due to experimental constraints. (b) ΔCPD(0) shows a linear dependence on layer thickness. Each data point is the average of two measurements. The inset in (b) shows how an exponential fit to the ΔCPD vs time profile is used to determine ΔCPD(0), based on the capacitor decay profile: $V(t) = V(0)e^{t/RC}$, where 1/RC is the decay rate constant. See further discussion in section 3.4 below.

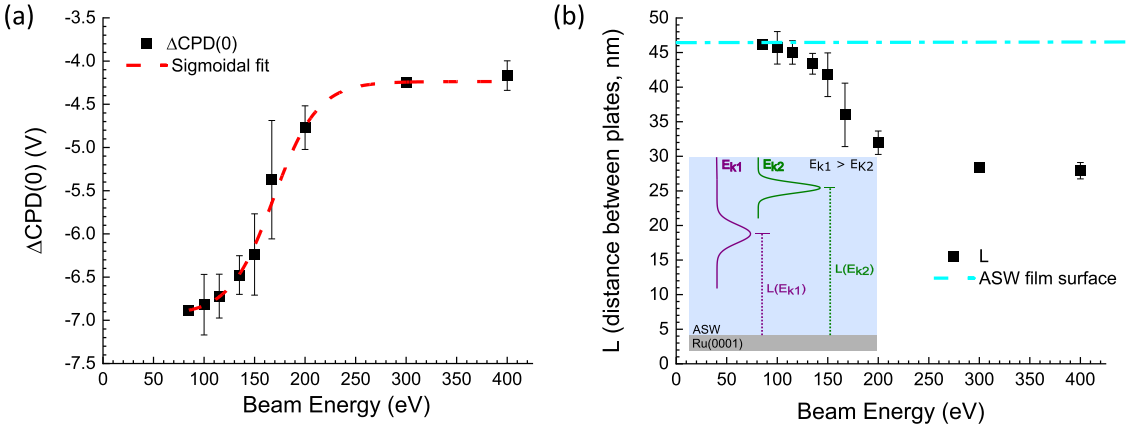

Figure 3. Beam energy effect on charge penetration. (a) ΔCPD(0) decreases (becomes less negative) along a sigmoidal curve with increasing beam energy. Each data point is the average of two measurements. (b) Calculated distance between the plates (L, in nanometers) as a function of beam energy. The dashed blue line represents the ASW film surface where the film thickness is 46.5 nm. The inset in (b) shows the (predicted) location of the charged layers for two different beam energies resulting in different effective penetration depths.

It has been previously demonstrated that the positive charging of ASW films follows a classical plate capacitor model[8,14,18] described by

$$\Delta V = \frac{QL}{A\varepsilon_0\varepsilon_{(T)}} \tag{1}$$

where ΔV is the measured ΔCPD, Q is the accumulated (positive) charge, L is the thickness of the ASW film, A is the area of the film exposed to the impinging charges, ε_0 is the vacuum permittivity, and $\varepsilon_{(T)}$ is the static dielectric constant of the material between the plates (reported to be 3.2 for ASW[26,28,29]). The strength of the electric field generated inside the ASW film can be calculated from the following equation

$$E = \frac{\Delta V}{L} \tag{2}$$

The thickness of the ASW film (L) is usually reported in monolayers (ML) of water adsorbed on the ruthenium substrate. For both crystalline and ASW films, 1ML = s = 0.37 nm.[30,31] This conversion assumes that the ASW film is compact. Initially, water molecules grow as islands.[32] At low temperatures where molecular reorientation is limited, island growth promotes porosity within the film. For porous films grown at temperatures below 115 K,[33] the film thickness can be calculated as follows

$$L = L_c\frac{\rho_c}{\rho(T_{gr})} = (\text{number of monolayers})s\frac{\rho_c}{\rho(T_{gr})} \tag{3}$$

where L is the actual film thickness in ML, L_c is the compact film thickness in ML, ρ_c is the density of a compact film, $\rho(T_{gr})$ is the growth temperature-dependent density of the porous film,[33] and s is the thickness of a compact monolayer in nanometers. Throughout this paper, experimental conditions will be reported in L_c to retain uniformity. When calculations concerning length are conducted, the actual length, L (after conversion to nanometers), will be used.

The results presented below are divided into two sections: first, the positively charged ASW film is characterized and its nanocapacitor properties are studied. The effects of ASW layer thickness, Ne^+ ion beam energy, and irradiation time (t_{irr}) on the measured ΔCPD and the generated electric field are investigated. Second, the effects of growth temperature (T_{gr}) and irradiation temperature (T_{irr}) on the nature of the proton

https://dx.doi.org/10.1021/acs.jpcc.0c07969
J. Phys. Chem. C 2020, 124, 23270−23279

traps, their thermal binding energies, and their stability are evaluated.

3.2. ASW Layer Thickness and Ne^+ Ion Beam Energy Effects on Film Charging. A linear dependence of ΔCPD(0) on film thickness is demonstrated when ASW films of varying thicknesses (100−3000 ML) are grown and bombarded at 35 K with Ne^+ (1.28×10^{11} collisions/s) for 10 s (Figure 2b). Measurements at a layer thickness of 3000 ML deviate from linearity, suggesting that the parallel-plate capacitor model gradually becomes less accurate for such thick films. For thicknesses between 100 and 2000 ML, the resulting nanocapacitor complies with the parallel-plate capacitor equation. The ΔCPD(0) cannot be measured directly as geometric constraints of the system only allow for ΔCPD measurements 4.5 min after the charging process is completed. The ΔCPD(0) is therefore defined by fitting each ΔCPD versus time curve (Figure 2a) to an exponential fit and extrapolating to $t = 0$ (inset Figure 2b). The stability of the ASW film charging is evaluated by measuring the ΔCPD over a 20 min period upon the completion of the charging process (Figure 2a). The stability of the charges is practically independent of the layer thickness. Over the 20 min measurement period, the ΔCPD decreases by ∼10% for all measured thicknesses.

The location of the charged layer (assuming a well-defined layer) within the ASW film is dictated by the Ne^+ ion beam energy. The beam energy determines whether the ions will be soft-landed on the water−vacuum interface or penetrate the film and form a charged layer below the surface. Beam energies ranging from 85 to 400 eV were investigated by bombarding 100 ML (46.5 nm) thick films grown at 35 K with Ne^+ ions at a fixed rate of 1.28×10^{11} collisions/s for 300 s. Figure 3a shows a sigmoidal relationship between the beam energy and ΔCPD(0). The charges penetrate further into the film at higher beam energies, bringing the distance between the charged layer and the ruthenium substrate closer together (see the scheme in the inset of Figure 3b). This is indicated by a drop in the measured ΔCPD(0), which can be well explained by the parallel-plate capacitor equation. The distance between the charged layer and the ruthenium substrate was calculated for all beam energies using eq 1 in section 3.1. In order to find the number of charges (Q) (which was assumed to be the same for each beam energy), the sigmoidal fit shown in Figure 3a was used to extrapolate the voltage at beam energy = 0 eV, where the charges would definitely reside on the ASW−vacuum interface. Using this voltage and the distance between the plates as defined by the ASW layer thickness (in nanometers), Q can be calculated. Once the fixed number of charges (Q) is known, the effective distance between the plates (L) (Figure 3b) and the penetration depth of charges can be derived for each beam energy. Figure 3b shows that at 85 eV, charge penetration of only 0.4 nm is observed (about 1 ML ASW below the water−vacuum interface). At 400 eV, the charges penetrate about 50 ML (19 nm) into the film. The charged layer remains close to the ASW film−vacuum interface up to a beam energy of 150 eV. It is important to note that this analysis cannot estimate the profile or distribution of the charged layer following its penetration into the ASW film and its stabilization. Therefore, we use the most probable distance as shown in the inset of Figure 3b.

3.3. Irradiation Time (t_{irr}) Effect. The irradiation time (t_{irr}) defines the number of Ne^+ ions that bombard the ASW film. Since the film voltage is proportional to the number of trapped charges (eq 1), it can be tuned by varying t_{irr}. Figure 4 shows that ΔCPD(0) increases exponentially (more negative

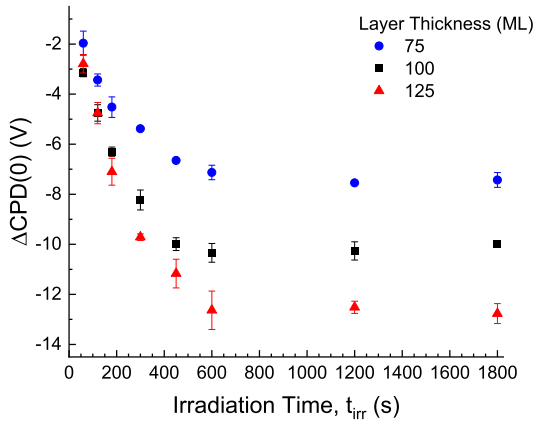

Figure 4. Effect of irradiation time on ΔCPD(0). ΔCPD(0) plotted vs time of Ne^+ ion bombardment (85 eV, 8 nA) at the indicated ASW film thickness in ML. Each data point is the average of two measurements.

ΔCPD(0)) with increasing t_{irr} for ASW films grown and bombarded at 35 K by a fixed Ne^+ ion flux of 1.28×10^{11} collisions/s. A plateau is reached at t_{irr} = 600 s for 75 ML (34.9 nm), 100 ML (46.5 nm), and 125 ML (58.1 nm) thick films after which no further charging is possible. The incoming excess charges most likely displace charges that are already trapped in the ASW film, initiating a cascade of charge hopping, which enables a steady positive current measurement. No retardation of the impinging ions back to the vacuum is expected since the maximum film charging is in the range of −7 to −13 V, while the ions hit the ASW film at an energy of 85 eV. There may be a space-charge effect taking place within the charged layer itself if the distribution of the charged layer is narrow. While the maximum ΔCPD(0) values depend on the ASW film thickness, the maximum number of trapped charges remains constant. Capacitance (C) is expected to be inversely proportional to the film thickness and is given by

$$C = \frac{A\varepsilon_0\varepsilon_{(T)}}{L} \tag{4}$$

These results indicate that the capacitance does not determine the maximum charge capacity for the ASW films. The electric field (see eq 2) is expected to be larger for thinner films that have higher capacitances. Here, the electric fields (E) generated within these films, where $Q = 4 \times 10^{-7}$ C, remain constant at $E = 2\ (\pm 1) \times 10^8$ V/m for film thicknesses of 75, 100, and 125 ML. This suggests that the maximum capacity is defined by the dielectric strength of the ASW film, which does not allow the electric field to exceed 2×10^8V/m. We found that t_{irr} does not affect the stability of the charges trapped in the ASW films.

3.4. Growth Temperature (T_{gr}) Effect. It is known that the morphology of ASW films is strongly affected by, and to some extent, controlled by the growth temperature (T_{gr}).[19,23,34−36] ASW films become more porous as the growth temperature is lowered. Higher growth temperatures (above 115 K but lower than 145 K where crystallization occurs) lead to the formation of compact amorphous films. This section will describe the effect of morphology on proton trapping, stability, and the structure of the proton binding site.

https://dx.doi.org/10.1021/acs.jpcc.0c07969
J. Phys. Chem. C 2020, 124, 23270−23279

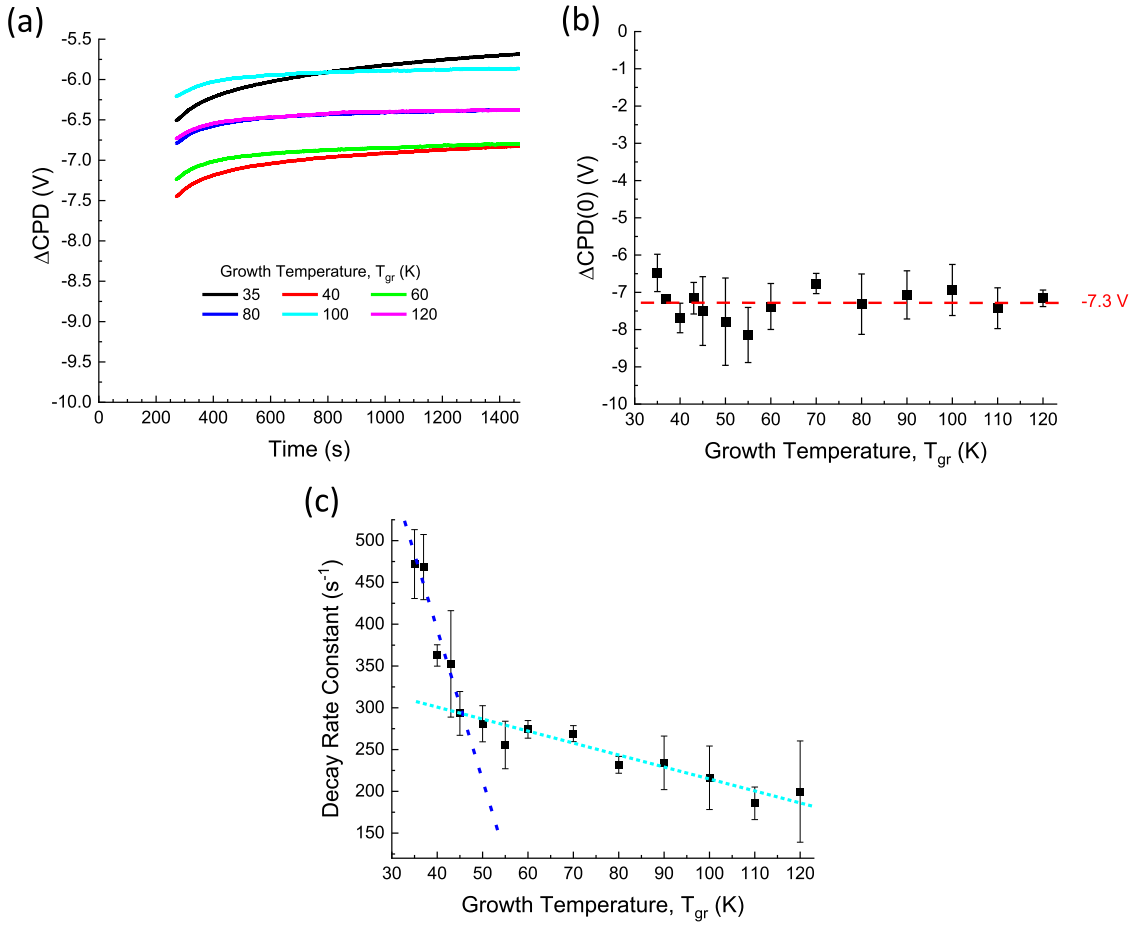

Figure 5. Morphology dependence on charge level and stability. 100 ML thick ASW films grown at the indicated T_{gr} and bombarded with Ne^+ ions (85 eV, 8 nA) for 180 s at 35 K, (a) ΔCPD versus time post Ne^+ ion bombardment and (b) ΔCPD(0) plotted as a function of T_{gr}. (c) Decay rate constants as a function of T_{gr}. Dashed lines are presented to guide the eye. Data points in (b) and (c) are the average of three measurements.

ASW films of 100 ML thickness were grown at varying T_{gr} (35−120 K) and then cooled down to 35 K before bombardment with Ne^+ ions (1.28×10^{11} collisions/s) for 180 s. The ΔCPD(0) values are unaffected by T_{gr} (within 10%), as seen in Figure 5b, and are centered around −7.3 V. This indicates that the film's morphology does not affect the number of impinging charges that can be trapped in the film.

While ΔCPD(0) remains constant over the T_{gr} range investigated, the stability of the trapped charges is clearly affected by the film morphology (see Figure 5a,c). The stability was determined by measuring the ΔCPD of the charged film for a duration of 20 min. Over this period, the CPD decreases (becomes less negative) as charges slowly migrate to the substrate. Overall, the charges are stably bound to the ASW films. The maximum decay in the ΔCPD amplitude was only by 14% over a 20 min period for films grown at 35 K. The stability of the charges increases with increasing T_{gr}, which is seen as a decrease in the decay rate of the charges (Figure 5c). The decay rate is measured by fitting the changes in ΔCPD over time with an exponential equation (eq 5) representing the discharge of a capacitor

$$V = V_0 e^{-t/RC} \tag{5}$$

where V is the voltage across the capacitor, V_0 is the maximum applied voltage, t is the time elapsed since the removal of voltage application (termination of the charging process), and RC is the time constant. The decay rate is defined as 1/RC, which is reported in units of s^{-1}. For T_{gr} = 35 K, the decay rate is 470 ± 40 s^{-1}, compared to 200 ± 60 s^{-1} for T_{gr} = 120 K. Figure 5c shows a fast, linear drop in the decay rate between T_{gr} = 35−50 K, and a slower linear decline is observed in the range of T_{gr} = 60−120 K. A similar behavior in charge stability was reported for negative charging of ASW films with electrons.[23]

The morphology affects the nature of the positive charge trapping sites. In a temperature-programmed contact potential difference (TP-ΔCPD) experiment, the ΔCPD of the ASW film is measured as the film temperature increases at a constant rate of 1 K/s. Changes in the macroscopic polarity of the film and water desorption from the substrate are reflected as changes in ΔCPD (Figure 6a). The temperature derivative of the TP-ΔCPD profile shown in Figure 6b shows the characteristic peaks for ASW films, which reflect reconstruction within the film and desorption: the peak at 159 K is attributed to multilayer desorption, while the peaks at 175 and 213 K are associated with desorption of the first monolayer of water.[23,37] An additional, much larger peak appears below 140 K, which is associated with the discharge of the film. In the low T_{gr} region (35−60 K), the discharge temperature increases with increasing T_{gr} and appears as a single, broad peak. From T_{gr} = 70 K, a low temperature shoulder can be resolved in addition to the main peak that gradually shifts upward with increasing T_{gr}. The discharge peak is correlated with the thermal binding energies of the charges to the ASW film. The main peak was

https://dx.doi.org/10.1021/acs.jpcc.0c07969
J. Phys. Chem. C 2020, 124, 23270−23279

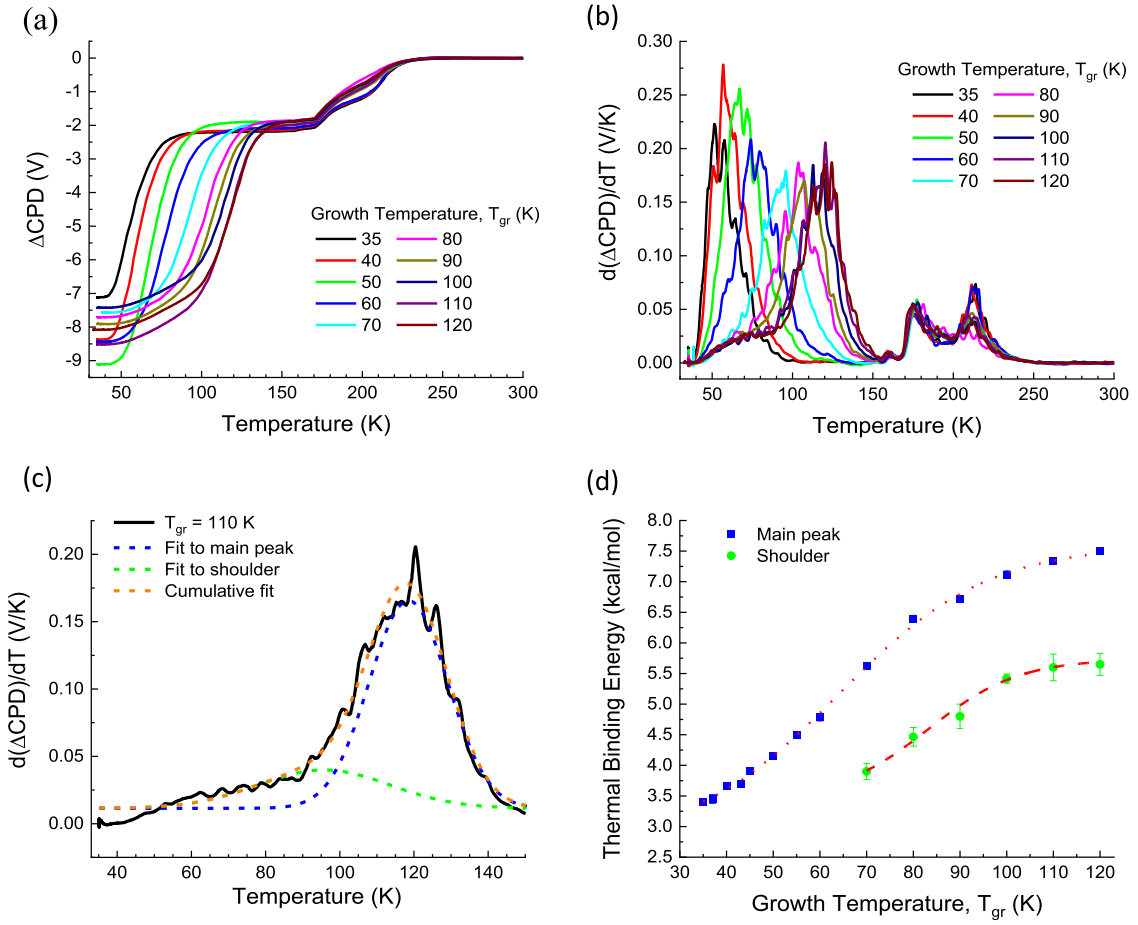

Figure 6. Thermal binding energy dependence on morphology. 100 ML thick ASW films grown at the indicated T_{gr} and irradiated with Ne^+ (85 eV, 8 nA) for 180 s, (a) TP-ΔCPD spectra with a heating rate of 1 K/s. (b) d(ΔCPD)/dT profiles of the graphs presented in (a). (c) Fit of the Gaussian peaks to the d(ΔCPD)/dT profile at T_{gr} = 110 K, illustrating how the shoulder and main discharge peaks were determined (the orange dashed line is the sum of both Gaussian peaks). (d) Apparent thermal binding energies as a function of T_{gr} obtained using a Redhead-like analysis of the peaks observed in the d(ΔCPD)/dT graph. The red dotted and dashed lines represent a sigmoidal fit to the data, to guide the eye. Each data point is the average of three measurements.

separated from the shoulder by fitting each d(ΔCPD)/dT versus temperature plot to a Gaussian profile as shown in Figure 6c. Each of the Gaussian fits was used in a Redhead-like desorption profile analysis[38] in order to extract an apparent binding energy of the charges to the ASW trapping sites. Figure 6d shows that the thermal binding energies of both the shoulder and the main discharge peak increase with increasing T_{gr} along a sigmoidal curve. The calculated thermal binding energies range from 3.4 to 7.5 Kcal/mol for the main peak and from 3.9 to 5.6 Kcal/mol for the shoulder.

We propose that the protons or hydronium ions (H_3O^+) are trapped in either L-defect sites or low-coordinated defect sites comprised of two- and three-coordinated water molecules. The type of site a proton becomes bound to is dependent on T_{gr} or the film morphology. In crystalline ice ($T_{gr} \geq 150$ K), the water molecules are arranged in a tetrahedral structure, forming four hydrogen bonds. At the ice surface, the water molecules have a lower coordination number, and therefore, cannot form four hydrogen bonds. Porous ASW films have a larger surface area,[34] and therefore, also contain more water molecules that are not fully coordinated. The coordination number of water molecules in ASW has been studied both theoretically[39−42] and experimentally[36,43,44] over a temperature range of 20−140 K. Infrared absorption spectra show that ASW clusters and films grown at low temperatures display two types of absorption peaks for dangling OH bonds (a doublet at 3720 and 3693 cm^{-1}).[42] These peaks are associated with two- and three-coordinated water molecules. Upon annealing to 60 K, the peak associated with the two-coordinated water molecules (3720 cm^{-1}) significantly decreases and three-coordination becomes dominant. Upon annealing to 120 K, both peaks decrease as the structure becomes more compact and contains more four-coordinated water molecules. Horimoto et al.[45] suggested that these morphological changes are associated with two types of structural defects: cavities containing large amounts of two-coordinated water molecules that collapse at 60 K and micropores that collapse at 120 K.

The thermal binding energies reported here reflect the morphological changes in the ASW film over the temperature range of 35−120 K. The thermal binding energies reflect the strength of the interaction between a proton and its binding site. The sigmoidal shape of the dependence of the thermal binding energy on growth temperature can be explained by looking at the temperature ranges at which drastic morphological changes take place in the ASW films. The inflection point of the sigmoidal function for the thermal binding energies of the main peak occurs at 64 K. Cavity collapse associated with a significant decrease in two-coordinated water

https://dx.doi.org/10.1021/acs.jpcc.0c07969
J. Phys. Chem. C 2020, 124, 23270−23279

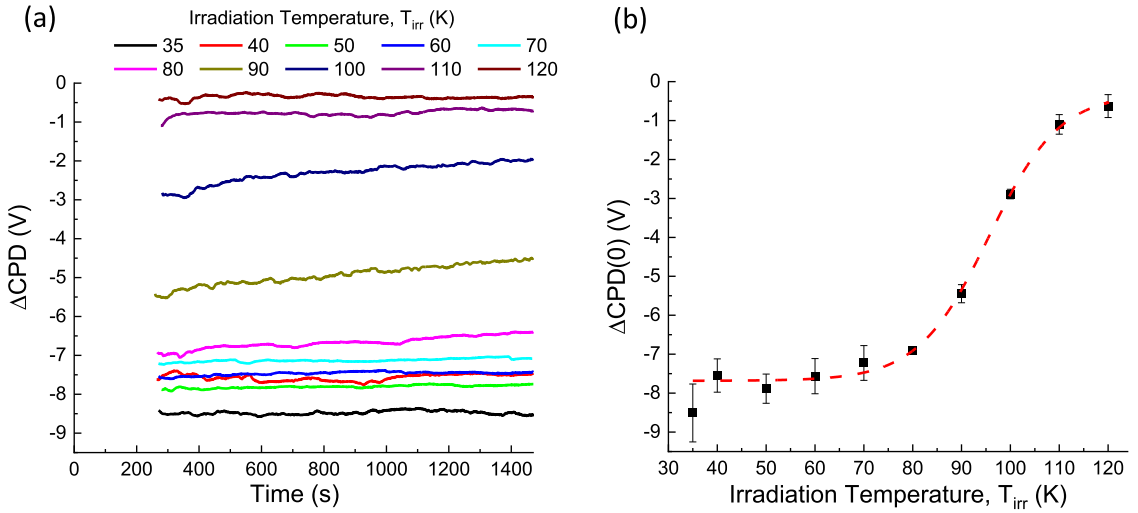

Figure 7. 100 ML thick ASW films grown at 120 K and irradiated with Ne^+ (85 eV, 8 nA) for 180 s at the indicated T_{irr}, (a) postirradiation ΔCPD versus time measurement and (b) ΔCPD(0) as a function of T_{irr}. The red-dashed line represents the sigmoidal fit discussed above. Each data point is the average of two measurements.

molecule defect sites indeed occurs at ~60 K.[45] The inflection point of the sigmoidal function for the thermal binding energies of the shoulder occurs at 83 K, which may be associated with the onset of micropore reconstruction (mentioned above[45]) where the film becomes more compact and water molecules are increasingly three- and four-coordinated.

For T_{gr} = 35−60 K, two- and three-coordinated water molecules are present. In this temperature range, the two-coordinated water molecules are thought to be dominant. This is reflected by the lower thermal binding energies (3.4−4.8 kcal/mol) in this region and the relatively broad peak in the d(ΔCPD)/dT profile (Figure 6b). As the growth temperature increases to 60 K, the number of two-coordinated water molecule defect sites decreases. This is reflected by the rise in the thermal binding energy as the protons are bound more strongly to the three-coordinated defect sites that have become more abundant. Above 60 K, there is a significant decrease in the amount of two-coordinated water molecules as there are no more cavities and only micropores are present. This is reflected in the d(ΔCPD)/dT profiles as a shift of the main peak to higher temperatures and the appearance of a temperature shoulder when $T_{gr} \geq 70$ K. The two peaks represent two types of proton binding sites. The low-temperature shoulder is correlated with low thermal binding energies (3.9−5.65 kcal/mol) associated with a mixture of two- and three-coordinated water molecules. The high-temperature main discharge peak is apparently associated with the trapping of protons in three- and four-coordinated (L-defect) water molecule defect sites. Each thermal binding energy represents a distribution of defect sites (explained by the relatively wide peaks in the d(ΔCPD)/dT spectra), and the energy for each single site cannot be differentiated. As T_{gr} increases from 70 to 120 K and the ice film becomes less porous, the relative amount of three- and four-coordinated water molecules increases.[36,39,46] This is reflected by an increase in the main peak thermal binding energy. At 120 K, when the ASW film is even more compact, the dominant thermal binding energy is 7.5 kcal/mol. Since an L-defect site has a binding energy of 10 kcal,[47] the binding energy of 7.5 kcal/mol may be assigned to the distribution of three- and four-coordinated (L-defect) water molecule defect sites.

The strength of the proton−defect interaction also affects the stability of the proton in the trap. In crystalline water ices, a proton thermodynamically prefers to reside at the surface where the water molecules are undercoordinated.[48] The four-coordinated water molecules in the bulk repel the hydronium ion, allowing for proton transport to occur toward the surface. For a proton to become trapped in the water ice interior, it must be sufficiently stable thermodynamically. In ASW, it is evident that there are different types of traps, as described above. The strongest and most stable trap is an L-defect where the water molecule is four-coordinated but oriented in such a way that two partially negative oxygens are facing each other creating a strong trap for a positive charge. The three-coordinated water molecules provide a very stable proton trap. Each hydrogen in the hydronium ion is hydrogen-bonded to an oxygen of another water molecule. When a proton is trapped in a two-coordinated water molecule site, the stabilization of the proton (H_3O^+) by two hydrogen bonds is weaker than in the three-coordinated site. Therefore, less energy is required for the proton to hop to a different water molecule along a two-coordinated water molecule network. This can explain the lower stability (higher decay rate) observed for low growth temperatures (<60 K), as seen in Figure 5c, where two-coordinated water molecule defect sites are dominant. At these low growth temperatures, the energy barrier for proton hopping along the two-coordinated water molecule network is lower than for films where three-coordination is dominant. This explains why the charge stability and thermal binding energy is lowest for ASW films grown at 35 K, where the two-coordinated defect sites are dominant. Figure 5c shows that as the growth temperature increases, the charge stability also increases. This is consistent with the increase in thermal binding energies.

3.5. Irradiation Temperature Effect (T_{irr}). To study the effects of T_{irr}, compact ASW films were grown at 120 K and bombarded with Ne^+ (1.28×10^{11} collisions/s) for 180 s at temperatures between 35 and 120 K. The ΔCPD is highest (most negative value) for films irradiated at the lowest temperature of 35 K (Figure 7a,b). As T_{irr} increases, the

https://dx.doi.org/10.1021/acs.jpcc.0c07969
J. Phys. Chem. C 2020, 124, 23270−23279

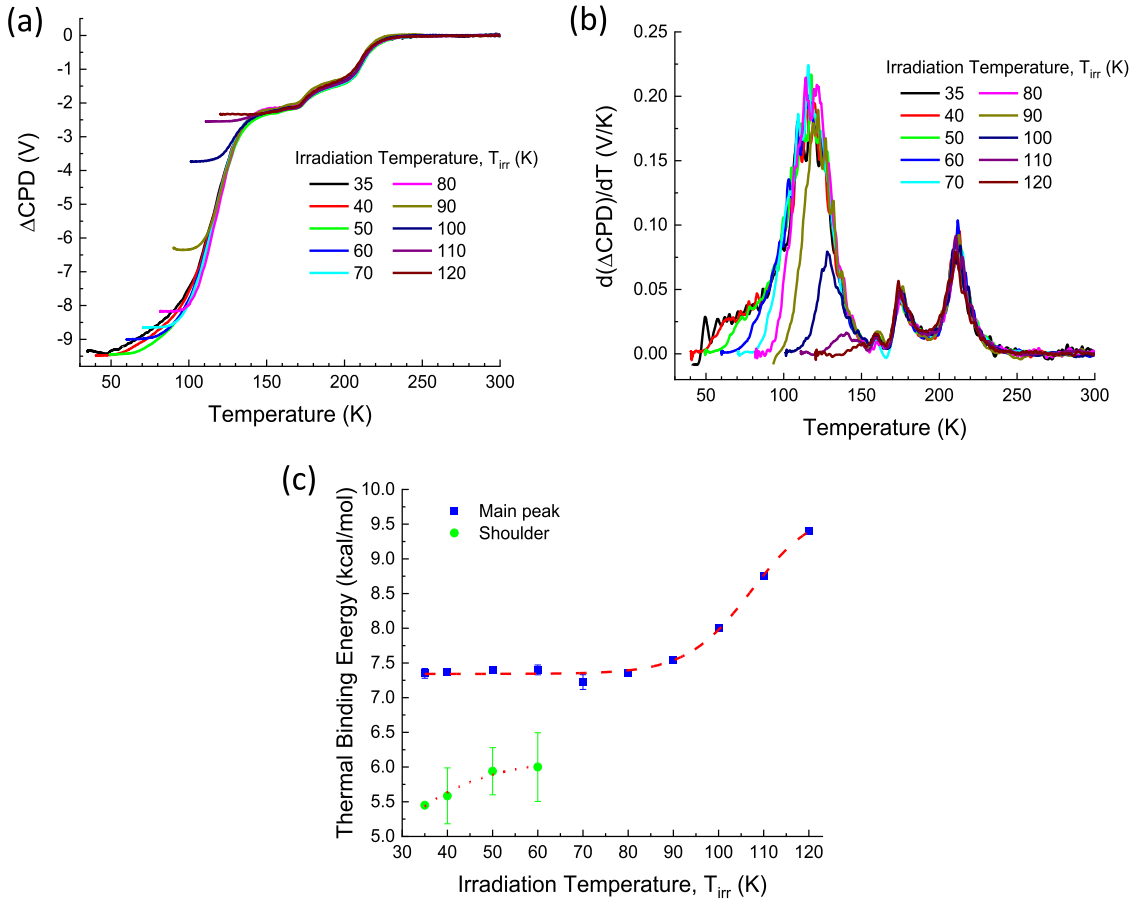

Figure 8. 100 ML thick ASW films grown at 120 K and bombarded with Ne^+ (85 eV, 8 nA) at the indicated T_{irr} for 180 s, (a) TP-ΔCPD profiles with a heating rate of 1 K/s and (b) temperature-derivative d(ΔCPD)/dT profiles for the spectra shown in (a, c); thermal binding energies corresponding to each T_{irr} are represented by blue squares for the main discharge peak and green circles for the shoulder. The red-dotted lines are to guide the eye. Data points are the average of two measurements.

ΔCPD of the film decreases (less negative values), following a sigmoidal curve, until the ΔCPD is almost zero at 120 K. From 80 to 100 K, the number of trapped charges and their stability decrease rapidly as charge transmission becomes dominant (Figure 7a).

These results suggest that the water molecules in the film start gaining mobility around 80 K and are fully mobile by 120 K. The sigmoidal relationship between the irradiation temperature and ΔCPD(0), shown in Figure 7b, can be associated with the proton mobility, which goes from a state of almost zero mobility (below 80 K) to a state of fast mobility (above 110 K). The transition between the two states is observed between 80 and 110 K with an inflection point at 95 K. It has previously been reported that water molecules only begin to reorient themselves in an ASW film from 125 K.[49] Here, increased proton mobility is already seen at 80 K. This behavior was also observed in previous studies where ASW films were charged with low-energy electrons[23] and with high-energy Ar^+.[17] It is possible that the charging process, where an internal field is developed, allows for reorientation of water molecules to occur at a lower temperature than previously reported. As the T_{irr} increases, proton transmission becomes dominant over proton trapping.

The TP-ΔCPD profiles and their d(ΔCPD)/dT spectra provide information regarding the thermal binding energies of the protons to the ASW film for T_{irr} = 35−120 K following growth at 120 K (compact film) (Figure 8a−c). For T_{irr} = 35−60 K, two peaks are apparent in the d(ΔCPD)/dT graph, which can be correlated with a low thermal binding energy site (5.45−6.0 kcal/mol) and a high thermal binding energy site (7.4 kcal/mol). The shoulder shifts to higher discharge temperatures as the T_{irr} increases until it disappears at 70 K. The main discharge peak remains unchanged in this temperature region. From 70 to 120 K, only one peak, corresponding to a high thermal binding energy (7.2−9.4 kcal/mol), is observed. As the T_{irr} increases, the peak discharge temperature increases while the peak width and intensity decrease.

As explained in the previous section, the thermal binding energies correspond to different types of proton traps (two-, three-, and four-coordinated water molecule defect sites) within the film. For low Ne^+ ion irradiation temperatures (≤ 60 K), protons can become trapped in two-, three-, and four-coordinated defect sites. The two distinct thermal binding energies reflect the wide distribution of the thermal binding energies for a film grown at 120 K and irradiated at low temperatures. As the T_{irr} increases, the protons become more mobile and are only trapped in sites where they are strongly bound. From T_{irr} = 70 K, protons are no longer bound in the weaker two-coordinated defect sites, which is reflected by a thermal binding energy of 7.2 ± 0.1 kcal/mol.

As the T_{irr} increases above 70 K, the trapping site distribution becomes narrower as less protons are trapped in the two and three-coordinated defect sites. At T_{irr} = 120 K, the few protons that are trapped have a thermal binding energy of

https://dx.doi.org/10.1021/acs.jpcc.0c07969
J. Phys. Chem. C 2020, 124, 23270−23279

9.4 kcal/mol, which probably corresponds to protons trapped in the L-defect sites for which a thermal binding energy of ~10 kcal/mol[47] has previously been reported.

4. CONCLUSIONS

Positive charging of ASW films grown on a Ru(0001) substrate by low-energy Ne^+ ions leads to the formation of a stable nanocapacitor. The charged layer is located slightly (0.4 nm) beneath the film−vacuum interface and is comprised of hydronium ions that are formed through a charge-transfer mechanism that occurs following Ne^+ ion impingement. The protons (H_3O^+) are trapped in either undercoordinated water molecule defect sites or L-defect sites, depending on the growth temperature of the film. The stability of the charges is affected by both the growth temperature of the ASW film and the irradiation temperature. The protons are most stable (low decay rate and high thermal binding energy) when trapped in ASW films grown at higher temperatures and irradiated at low temperatures. From irradiation temperatures of 80 K, the protons in the ASW films gain mobility, and proton transmission is promoted over proton trapping. The range of the thermal binding energies presented here (3.4−9.4 kcal/mol) is similar to the range reported for ASW films charged with low-energy electrons (4−8 kcal/mol).[23] Additionally, activation energies in the range of 2.7−8.6 kcal/mol were also observed for the depolarization of neutral ASW films (T_{gr} = 33−115 K) upon annealing.[50] This suggests that the binding strength of charges to ASW films, whether positively charged protons or negatively charged electrons, is highly sensitive to and actually depends on the changes in film porosity that occur during annealing. Electric fields of 2 (± 1) × 10^8 V/m are generated within the ASW films. This work forms the foundation for further study of chemical processes occurring on icy grains in the ISM. The influence of electric fields on the chemistry of the ISM is yet to be explored.

AUTHOR INFORMATION

Corresponding Author

Micha Asscher − *Institute of Chemistry, The Hebrew University of Jerusalem, Jerusalem 9190401, Israel;* orcid.org/0000-0002-4476-5617; Email: micha.asscher@mail.huji.ac.il

Authors

Michelle Akerman − *Institute of Chemistry, The Hebrew University of Jerusalem, Jerusalem 9190401, Israel*

Roey Sagi − *Institute of Chemistry, The Hebrew University of Jerusalem, Jerusalem 9190401, Israel*

Complete contact information is available at: https://pubs.acs.org/10.1021/acs.jpcc.0c07969

Notes

The authors declare no competing financial interest.

ACKNOWLEDGMENTS

Partial support by the Israel Science Foundation (ISF, grant number 52/14) and by the Einstein Foundation Berlin is acknowledged. The critical technical support provided by the Physics workshop staff (Avner and Rowe) and the Electronics workshop staff (Eduard, Marcelo, Shaul, and Alex) is greatly appreciated.

REFERENCES

(1) Sandford, S. A. The Inventory of Interstellar Materials Available for the Formation of the Solar System. *Meteorit. Planet. Sci.* **1996**, *31*, 449−476.

(2) Öberg, K. I. Photochemistry and Astrochemistry: Photochemical Pathways to Interstellar Complex Organic Molecules. *Chem. Rev.* **2016**, *116*, 9631−9663.

(3) Greenberg, J. M. Radical Formation, Chemical Processing, and Explosion of Interstellar Grains. *Astrophys. Space Sci.* **1976**, *39*, 9−18.

(4) Sorrell, W. H. Origin of Amino Acids and Organic Sugars in Interstellar Clouds. *Astrophys. J.* **2001**, *555*, L129−L132.

(5) Stuyver, T.; Danovich, D.; Joy, J.; Shaik, S. External Electric Field Effects on Chemical Structure and Reactivity. *WIREs Comput. Mol. Sci.* **2020**, *10*, No. e1438.

(6) Shaik, S.; Danovich, D.; Joy, J.; Wang, Z.; Stuyver, T. Electric-Field Mediated Chemistry: Uncovering and Exploiting the Potential of (Oriented) Electric Fields to Exert Chemical Catalysis and Reaction Control. *J. Am. Chem. Soc.* **2020**, *142*, 12551−12562.

(7) Shaik, S.; Ramanan, R.; Danovich, D.; Mandal, D. Structure and Reactivity/Selectivity Control by Oriented-External Electric Fields. *Chem. Soc. Rev.* **2018**, *47*, 5125−5145.

(8) Shin, S.; Kim, Y.; Moon, E.; Lee, D. H.; Kang, H.; Kang, H. Generation of Strong Electric Fields in an Ice Film Capacitor. *J. Chem. Phys.* **2013**, *139*, No. 074201.

(9) Park, Y.; Lim, J. H.; Lee, J. Y.; Kang, H. Electric Field Effect on Condensed-Phase Molecular Systems. VII. Vibrational Stark Sensitivity of Spatially Oriented Water Molecules in an Argon Matrix. *J. Phys. Chem. C* **2019**, *123*, 9868−9874.

(10) Shin, S.; Kim, Y.; Kang, H.; Kang, H. Effect of Electric Field on Condensed-Phase Molecular Systems. I. Dipolar Polarization of Amorphous Solid Acetone. *J. Phys. Chem. C* **2015**, *119*, 15588−15595.

(11) Gryn'ova, G.; Coote, M. L. Origin and Scope of Long-Range Stabilizing Interactions and Associated SOMO−HOMO Conversion in Distonic Radical Anions. *J. Am. Chem. Soc.* **2013**, *135*, 15392−15403.

(12) Klinska, M.; Smith, L. M.; Gryn'ova, G.; Banwell, M. G.; Coote, M. L. Experimental Demonstration of PH-Dependent Electrostatic Catalysis of Radical Reactions. *Chem. Sci.* **2015**, *6*, 5623−5627.

(13) Gryn'ova, G.; Coote, M. L. Directionality and the Role of Polarization in Electric Field Effects on Radical Stability. *Aust. J. Chem.* **2017**, *70*, 367−372.

(14) Tsekouras, A. A.; Iedema, M. J.; Cowin, J. P. Amorphous Water-Ice Relaxations Measured with Soft-Landed Ions. *Phys. Rev. Lett.* **1998**, *80*, 5798−5801.

(15) Cowin, J. P.; Tsekouras, A. A.; Iedema, M. J.; Wu, K.; Ellison, G. B. Immobility of Protons in Ice from 30 to 190 K. *Nature* **1999**, *398*, 405−407.

(16) Shi, J.; Famá, M.; Teolis, B. D.; Baragiola, R. A. Ion-Induced Electrostatic Charging of Ice. *Nucl. Instrum. Methods Phys. Res. B* **2010**, *268*, 2888−2891.

(17) Shi, J.; Famá, M.; Teolis, B. D.; Baragiola, R. A. Ion-Induced Electrostatic Charging of Ice at 15−160 K. *Phys. Rev. B* **2012**, *85*, No. 035424.

(18) Horowitz, Y.; Asscher, M. Low Energy Charged Particles Interacting with Amorphous Solid Water Layers. *J. Chem. Phys.* **2012**, *136*, 134701.

(19) Bu, C.; Baragiola, R. A. Proton Transport in Ice at 30−140 K: Effects of Porosity. *J. Chem. Phys.* **2015**, *143*, No. 074702.

(20) Simpson, W. C.; Orlando, T. M.; Parenteau, L.; Nagesha, K.; Sanche, L. Dissociative Electron Attachment in Nanoscale Ice Films: Thickness and Charge Trapping Effects. *J. Chem. Phys.* **1998**, *108*, 5027−5034.

(21) Michaud, M.; Wen, A.; Sanche, L. Cross Sections for Low-Energy (1−100 EV) Electron Elastic and Inelastic Scattering in Amorphous Ice. *Rare* **2003**, *159*, 3−22.

(22) Balog, R.; Cicman, P.; Field, D.; Feketeová, L.; Hoydalsvik, K.; Jones, N. C.; Field, T. A.; Ziesel, J.-P. Transmission and Trapping of Cold Electrons in Water Ice. *J. Phys. Chem. A* **2011**, *115*, 6820−6824.

(23) Sagi, R.; Akerman, M.; Ramakrishnan, S.; Asscher, M. Temperature Effect on Transport, Charging, and Binding of Low-Energy Electrons Interacting with Amorphous Solid Water Films. *J. Phys. Chem. C* **2018**, *122*, 9985−9996.
(24) Livneh, T.; Asscher, M. The Adsorption and Decomposition of C_2H_4 on Ru(001): A Combined TPR and Work Function Change Study. *J. Phys. Chem. B* **2000**, *104*, 3355−3363.
(25) *Atomic Data for Neon (Ne)* https://physics.nist.gov/PhysRefData/Handbook/Tables/neontable1.htm (accessed Jun 30, 2020).
(26) Joshipura, K. N.; Gangopadhyay, S.; Limbachiya, C. G.; Vinodkumar, M. Electron Impact Ionization of Water Molecules in Ice and Liquid Phases. *J. Phys.: Conf. Ser.* **2007**, *80*, No. 012008.
(27) Bag, S.; McCoustra, M. R. S.; Pradeep, T. Formation of H_2^+ by Ultra-Low-Energy Collisions of Protons with Water Ice Surfaces. *J. Phys. Chem. C* **2011**, *115*, 13813−13819.
(28) Pan, X.; Abdoul-Carime, H.; Cloutier, P.; Bass, A. D.; Sanche, L. D−, O− and OD−Desorption Induced by Low-Energy (0−20eV) Electron Impact on Amorphous D2O Films. *Radiat. Phys. Chem.* **2005**, *72*, 193−199.
(29) Herring-Captain, J.; Grieves, G. A.; Alexandrov, A.; Sieger, M. T.; Chen, H.; Orlando, T. M. Low-Energy (5 − 250 EV) Electron-Stimulated Desorption of H + , H 2 + , and H + (H 2 O) n from Low-Temperature Water Ice Surfaces. *Phys. Rev. B* **2005**, *72*, No. 035431.
(30) Thürmer, K.; Bartelt, N. C. Growth of Multilayer Ice Films and the Formation of Cubic Ice Imaged with STM. *Phys. Rev. B* **2008**, *77*, 195425.
(31) Dowell, L. G.; Rinfret, A. P. Low-Temperature Forms of Ice as Studied by X-Ray Diffraction. *Nature* **1960**, *188*, 1144−1148.
(32) Haq, S.; Hodgson, A. Multilayer Growth and Wetting of Ru(0001). *J. Phys. Chem. C* **2007**, *111*, 5946−5953.
(33) Berland, B. S.; Brown, D. E.; Tolbert, M. A.; George, S. M. Refractive Index and Density of Vapor-Deposited Ice. *Geophys. Res. Lett.* **1995**, *22*, 3493−3496.
(34) Mayer, E.; Pletzer, R. Astrophysical Implications of Amorphous Ice—a Microporous Solid. *Nature* **1986**, *319*, 298−301.
(35) Kimmel, G. A.; Stevenson, K. P.; Dohnálek, Z.; Smith, R. S.; Kay, B. D. Control of Amorphous Solid Water Morphology Using Molecular Beams. I. Experimental Results. *J. Chem. Phys.* **2001**, *114*, 5284−5294.
(36) Bu, C.; Shi, J.; Raut, U.; Mitchell, E. H.; Baragiola, R. A. Effect of Microstructure on Spontaneous Polarization in Amorphous Solid Water Films. *J. Chem. Phys.* **2015**, *142*, 134702.
(37) Lilach, Y.; Romm, L.; Livneh, T.; Asscher, M. The First Layers of Water on Ru(001). *J. Phys. Chem. B* **2001**, *105*, 2736−2742.
(38) Yates, J. T. *Experimental Innovations in Surface Science: A Guide to Practical Laboratory Methods and Instruments*; Springer-Verlag: New York, 1998.
(39) Buch, V. Identification of Two Distinct Structural and Dynamical Domains in an Amorphous Water Cluster. *J. Chem. Phys.* **1990**, *93*, 2631−2639.
(40) Zhang, Q.; Buch, V. Computational Study of Formation Dynamics and Structure of Amorphous Ice Condensates. *J. Chem. Phys.* **1990**, *92*, 5004−5016.
(41) Zhang, Q.; Buch, V. Condensation and Structure of Amorphous Ices: A Computational Study. *J. Chem. Phys.* **1990**, *92*, 1512−1513.
(42) Buch, V.; Devlin, J. P. Spectra of Dangling OH Bonds in Amorphous Ice: Assignment to 2- and 3-coordinated Surface Molecules. *J. Chem. Phys.* **1991**, *94*, 4091−4092.
(43) Raut, U.; Famá, M.; Teolis, B. D.; Baragiola, R. A. Characterization of Porosity in Vapor-Deposited Amorphous Solid Water from Methane Adsorption. *J. Chem. Phys.* **2007**, *127*, 204713.
(44) Rowland, B.; Fisher, M.; Devlin, J. P. Probing Icy Surfaces with the Dangling-OH-mode Absorption: Large Ice Clusters and Micro-porous Amorphous Ice. *J. Chem. Phys.* **1991**, *95*, 1378−1384.
(45) Horimoto, N.; Kato, H. S.; Kawai, M. Stepwise Morphological Change of Porous Amorphous Ice Films Observed through Adsorption of Methane. *J. Chem. Phys.* **2002**, *116*, 4375−4378.
(46) Buch, V. Growth and Structure of Amorphous Ice Condensates: A Computational Study. II. *J. Chem. Phys.* **1992**, *96*, 3814−3823.
(47) Wooldridge, P. J.; Devlin, J. P. Proton Trapping and Defect Energetics in Ice from FT-IR Monitoring of Photoinduced Isotopic Exchange of Isolated D_2O. *J. Chem. Phys.* **1988**, *88*, 3086−3091.
(48) Lee, C.-W.; Lee, P.-R.; Kang, H. Protons at Ice Surfaces. *Angew. Chem., Int. Ed.* **2006**, *45*, 5529−5533.
(49) Lee, C.-W.; Lee, P.-R.; Kim, Y.-K.; Kang, H. Mechanistic Study of Proton Transfer and H/D Exchange in Ice Films at Low Temperatures (100−140K). *J. Chem. Phys.* **2007**, *127*, No. 084701.
(50) Sagi, R.; Akerman, M.; Ramakrishnan, S.; Asscher, M. The Role of Thermal History on Spontaneous Polarization and Phase Transitions of Amorphous Solid Water Films Studied by Contact Potential Difference Measurements. *J. Chem. Phys.* **2020**, *153*, 144702.

https://dx.doi.org/10.1021/acs.jpcc.0c07969
J. Phys. Chem. C 2020, 124, 23270−23279